DRAFT VERSION DECEMBER 25, 2013
Preprint typeset using LATEX style emulateapj v. 12/14/05

DEEP U^*- AND G-BAND IMAGING OF THE *SPITZER SPACE TELESCOPE* FIRST LOOK SURVEY FIELD: OBSERVATIONS AND SOURCE CATALOGS

HYUNJIN SHIM[1,5], MYUNGSHIN IM[1,6], SOOJONG PAK[2,4], PHILIP CHOI[3], DARIO FADDA[3], GEORGE HELOU[3], & LISA STORRIE-LOMBARDI[3]

Draft version December 25, 2013

ABSTRACT

We present deep u^*-, and g-band images taken with the MegaCam on the 3.6 m Canada-France-Hawaii Telescope (CFHT) to support the extragalactic component of the *Spitzer* First Look Survey (hereafter, FLS). In this paper we outline the observations, present source catalogs and characterize the completeness, reliability, astrometric accuracy and number counts of this dataset. In the central 1 deg^2 region of the FLS, we reach depths of g ∼26.5 mag, and u^* ∼26.2 mag (AB magnitude, 5σ detection over a 3″ aperture) with ∼4 hours of exposure time for each filter. For the entire FLS region (∼5 deg^2 coverage), we obtained u^*-band images to the shallower depth of u^* =25.0–25.4 mag (5σ, 3″ aperture). The average seeing of the observations is 0.″85 for the central field, and ∼1.″00 for the other fields. Astrometric calibration of the fields yields an absolute astrometric accuracy of 0.″15 when matched with the SDSS point sources between 18< g <22. Source catalogs have been created using *SExtractor*. The catalogs are 50% complete and greater than 99.3% reliable down to $g \simeq 26.5$ mag and $u^* \simeq 26.2$ mag for the central 1 deg^2 field. In the shallower u^*-band images, the catalogs are 50% complete and 98.2% reliable down to 24.8–25.4 mag. These images and source catalogs will serve as a useful resource for studying the galaxy evolution using the FLS data.

Subject headings: catalogs—surveys—galaxies:photometry

1. INTRODUCTION

Since its launch in August 2003, the *Spitzer* space telescope has opened new IR observing windows to the universe and probed to unprecedented depths. The first scientific observation undertaken with the *Spitzer* after its in-orbit-checkout period was the *Spitzer* First Look Survey. The survey provided the first look of the mid-infrared (MIR) sky with deeper sensitivities than previous systematic large surveys[7], allowing future users to gauge *Spitzer* sensitivities. For the extragalactic component of the First Look Survey (FLS), the ∼4.3 deg^2 field centered at RA=17^{h}18^{m}00^s, DEC=+59°30′00″ was observed with the InfraRed Array Camera (IRAC, 3.6, 4.5, 5.8, 8.0μm; Fazio et al. 2004) and the Multiband Imaging Photometer for Spitzer (MIPS, 24, 70, 160μm; Rieke et al. 2004). The main survey field has flux limits of 20, 25, 100, and 100μJy at wavelengths of IRAC 3.6, 4.5, 5.8, and 8.0μm respectively. The deeper verification field, covering the central 900 arcmin^2 field, has sensitivities of 10, 10, 30, and 30μJy at IRAC wavelengths. (Lacy et al. 2005) Also, the FLS verification strip field has 3σ flux limits of 90μJy at MIPS 24μm (Yan et al. 2004a), and 9, and 60 mJy at 70, 160μm (Frayer et al. 2005). The reduced images and source catalogs have been released (Lacy et al. 2005; Frayer et al. 2005).

In order to support the FLS, various ground-based ancillary datasets have also been obtained. A deep R-band survey to $R_{AB}(5\sigma)$=25.5 mag (KPNO 4 m, Fadda et al. 2004) and a radio survey at 1.4GHz to 90μJy (VLA, Condon et al. 2003) have been performed to identify sources at different wavelengths. Imaging surveys with the Palomar Large Format Camera (LFC), g', r', i' and z' band data covering 1–4 deg^2 have also been taken since 2001. The Sloan Digital Sky Survey also covers the FLS field. Moreover, spectroscopic redshifts have been obtained for many sources using the DEep Imaging Multi-Object Spectrograph (DEIMOS) at the Keck observatory as well as Hydra instrument on the Wisconsin Indiana Yale NOAO (WIYN) observatory. Utilizing all the *Spitzer* and the ground-based ancillary datasets, many science results have come out already from the FLS. The FLS studies range from the infrared source counts to the properties of obscured galaxies such as submm galaxies, red Active Galactic Nuclei(AGNs), and Extremely Red Objects (e.g. Yan et al. 2004b; Fang et al. 2004; Marleau et al. 2004; Frayer et al. 2004; Appleton et al. 2004; Lacy et al. 2004; Choi et al. 2005).

In order to broaden the scientific scope of the FLS, we have obtained new ground-based ancillary datasets, deep u^*-band and g-band imaging data that will be presented in this paper. The exploration of the cosmic star formation history at $z \lesssim 3$ is one of the key scientific issues that the FLS is designed to address. While studying the infrared emission is an extremely valuable way to understand the obscured star formation history of the universe, a complete census of the cosmic star formation history requires the measurement of unobscured star formation as well. Such a measurement can be done effectively using the rest-frame ultraviolet (UV) continuum, which represents either instantaneous star formation activity of massive stars (Far UV; FUV), or traces the star formation from intermediate age stars (Near UV; NUV) (Kennicutt 1998). The FUV and NUV emission of galaxies at $z \lesssim 1$ redshifts to the u-band; therefore, the addition of the u-band enables us to describe the star formation history at $z \lesssim 1$ to the full extent. Also, using the deep u-band and g-band data, it is possible to select u-band dropout galaxies – star forming galaxies at $z \sim 3$. Especially of interest are bright, massive Lyman Break Galaxies which are rare, but important to constrain galaxy

[1] Dept. of Physics & Astronomy, Seoul National University, Seoul, Korea
[2] Korea Astronomy & Space Science Institute, Daejeon, Korea
[3] Spitzer Science Center, California Institute of Technology, Pasadena, CA 91125
[4] Dept. of Astronomy and Space Science, Kyung Hee University, Yongin-shi, Kyunggi-do 449-701, Korea
[5] hjshim@astro.snu.ac.kr
[6] mim@astro.snu.ac.kr
[7] See the First Look Survey website, http://ssc.spitzer.caltech.edu/fls

TABLE 1
CHARACTERISTICS OF THE FILTERS USED IN MEGACAM OBSERVATIONS

Filter	u^*	g
central wavelength (Å)	3740	4870
wavelength range	3370 – 4110	4140 – 5590
mean transmission (%)	69.7	84.6

evolution models since they can tell us how massive galaxies are assembled in the early universe. The wide area coverage of the FLS allows us to select such rare, bright LBGs. However, for the selection of LBGs, it is necessary to obtain *u*-band data and *g*-band data that matches the depth of the *Spitzer* data. In addition, the *u*-band and *g*-band datasets can be used to test extinction correction methods, such as the estimation of dust extinction based on the measurement of UV slope (Calzetti et al. 1994; Meurer et al. 1999; Adelberger & Steidel, 2000). When used together with other ground-based ancillary data, our *u*- and *g*-band data will be very helpful for improving the accuracy of photometric redshifts.

With these scientific applications in mind, we present the u^*- and *g*-band optical observations made with the MegaCam at Canada France Hawaii Telescope (CFHT). The dataset is composed of i) deep u^*-, *g*-band data for the central 1 deg^2 of the FLS, and ii) u^*-band data for the whole FLS. In §2, we describe how our observations were made. The reduction and calibration procedures are in §3. Production of source catalogs is described in §4. Finally in §5, we show the properties of the final images and the extracted catalogs. Throughout this paper, we use AB magnitudes (Oke 1974).

2. OBSERVATIONS

The observations were made using the MegaCam on the 3.6 m Canada France Hawaii Telescope (CFHT). MegaCam consists of 36 2048×4612 pixel CCDs, covering 0.96 deg×0.94 deg field of view with a resolution of 0.187″ per pixel (See the detailed description in Boulade et al. 2003). The available broad-band filters are similar to SDSS *ugriz* filters, but not exactly the same especially in the case of u^*-band. We used u^* and *g* filters for our observations. The filter characteristics are summarized in Table 1, and their response curves are compared to the SDSS *u*- and *g*-band filters in Figure 1. Note that these response curves include the quantum efficiency of the CCDs. The response curves of the two *g*-bands are nearly identical in their shapes, but the u^*-band response curve shows a different overall shape compared to the SDSS *u*-band, in such a sense that u^* filter is redder than SDSS *u*. The difference leads to as much as a 0.6 mag difference between the CFHT & SDSS *u*-magnitudes. This will be investigated further in the photometry section (§5.2).

Our images on the FLS field were taken with the queued observation mode in two separate runs (03B and 04A semesters). The first observing run occurred in August 23–29 (u^*-band) and September 19–22 (*g*-band), 2003. During this 03B run, we observed the central 1 deg^2 of the FLS field, which covers the entire FLS verification strip. Images are taken with medium dither steps of about 30″, at 12 (u^*) or 20 (*g*) different dither positions. The exposure time at each position was 1160 seconds for u^*-band, 680 seconds for *g*-band. Therefore, the total integration time per pixel amounts to ∼3.8 hours for both bands. The yellow-colored box in Figure 2, shows the location of this deep u^*- and *g*-band data superimposed on the

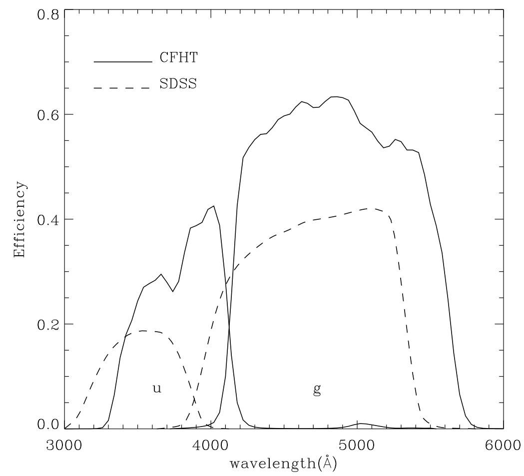

FIG. 1.— The response curves of CFHT u^*, *g* filters multiplied by the telescope (mirror, optics) and CCD efficiency (*solid*). The CFHT data points are taken from a CFHT-related homepage (http://astrowww.phys.uvic.ca/grads/gwyn/cfhtls). The SDSS *u*-, *g*-band transmission curves are given as *dashed* lines (http://www.sdss.org). The CFHT filters are slightly redder than their SDSS counterparts.

R-band images (Fadda et al. 2004).

In the second observing run during 04A period, we obtained u^*-band images covering the whole FLS field (∼5 deg^2) at a shallower depth. Note that we did not take *g*-band data because the entire FLS is covered to a shallower depth by the existing *g*-band data taken with the Palomar 5 m telescope. The CFHT observation was at first designed to take 10 dithered images at 7 different locations of the FLS area, which are named as FLS11–FLS32 (Table 2). The cyan-colored boxes marked with the dashed line in Figure 2 indicate FLS11–FLS32 fields. The dates when the observations made span quite a wide range from April to July 2004. Some of the fields have all dithered images observed on a photometric condition (FLS21, FLS22 & FLS31), but other fields contain the images that are non-photometric. Due to the bad weather, we lost some of the queued observing time and several observed images were not validated. Each dithered image was taken with the exposure time of 680 seconds. Although the original plan was to achieve 1.9 hours of total integration at each location, there is a field-to-field variation on the image depth between ∼1 hour and ∼2 hours. Table 2 gives the summary of the 03B and 04A observations. The seeing condition of the whole observation sessions ranged from 0.″85 to 1.″08.

Between August 2003 and September 2003, one of the 36 MegaCam CCDs was malfunctioning. As a result, *g*-band images lack [CCD03] part of the observed field. Hence, the effective survey area in coadded mosaic image is ∼0.94 deg^2 for the central field.

3. DATA REDUCTION

3.1. *Preprocessing with Elixir*

All MegaCam data obtained at CFHT are preprocessed through the Elixir pipeline[8], the standard pipeline for the basic reduction of the MegaCam data, provided by the CFHT. Through the Elixir pipeline, the raw object frames are bias subtracted, flat fielded, and photometrically calibrated. In the Elixir photometric calibration, the nightly photometric zero-point is estimated using the standard star data on that night.

[8] See Elixir website http://www.cfht.hawaii.edu/Instruments/Elixir

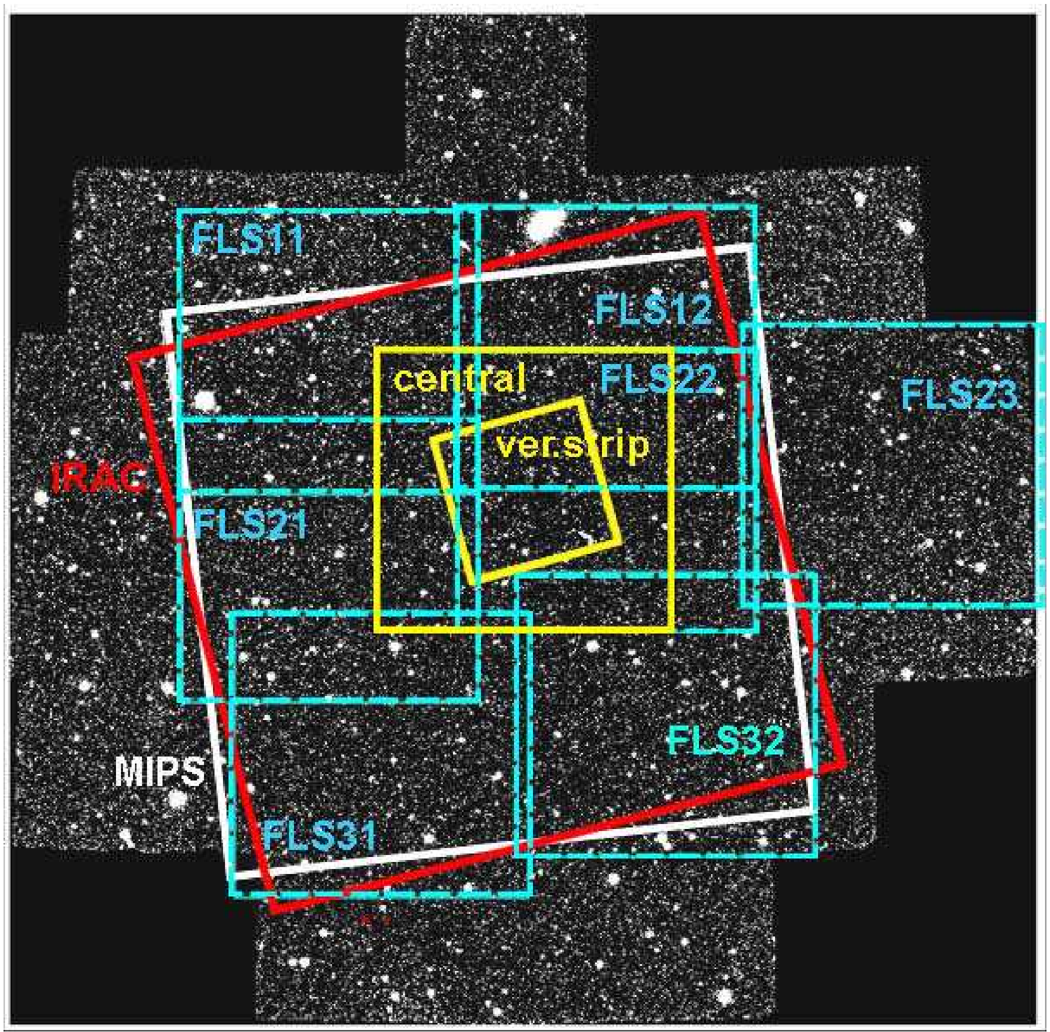

FIG. 2.— Area coverages of various datasets over the FLS. The small yellow square in the center represents the *Spitzer* FLS verification strip, and the big yellow square shows our CFHT observations in the central 1 deg^2. The red/white squares correspond to the whole FLS area (IRAC/MIPS respectively) which covers $\sim$4.3 deg^2. The cyan squares indicate the area covered by our CFHT u^*-band observations in 2004. All these marks are overlayed on the KPNO *R*-band images.

TABLE 2
OBSERVATION SUMMARY

Field ID	α (J2000)	δ (J2000)	Observation Dates	Filter	Total Exposure Time (sec)	Depth (AB mag)[a]	Seeing ($''$)[b]	Zeropoint[c]
central	17:17:01	+59:45:08	2003/08/25, 2003/08/29	u^*	1160 × 12	26.41	0.85	32.904
central	17:17:01	+59:45:08	2003/09/19, 2003/09/21, 2003/09/22	g	680 × 20	26.72	0.85	33.430
FLS11	17:22:09	+60:14:47	2004/04/29, 2004/07/12	u^*	680 × 10	25.83	0.98	32.226
FLS12	17:14:44	+60:14:50	2004/06/18, 2004/07/17	u^*	680 × 9	25.85	1.06	32.186
FLS21	17:22:14	+59:30:00	2004/07/10, 2004/07/21	u^*	680 × 9	25.91	0.98	32.236
FLS22	17:14:47	+59:44:45	2004/07/10	u^*	680 × 5	25.57	1.08	32.213
FLS23	17:07:09	+59:48:26	2004/07/11	u^*	680 × 5	25.43	0.89	32.221
FLS31	17:20:46	+58:49:09	2004/07/11, 2004/07/22	u^*	680 × 8	25.68	0.90	32.188
FLS32	17:13:32	+58:57:46	2004/07/12	u^*	680 × 7	25.67	0.95	32.139

[a]The depth of a field is calculated as 5σ flux over a $3''$ aperture.
[b]The seeing of the image was determined through a visual inspection on individual stars.
[c]The zeropoints are calibrated from original Elixir photometric solution (See §3.5). The values are given as zeropoints according to DN.

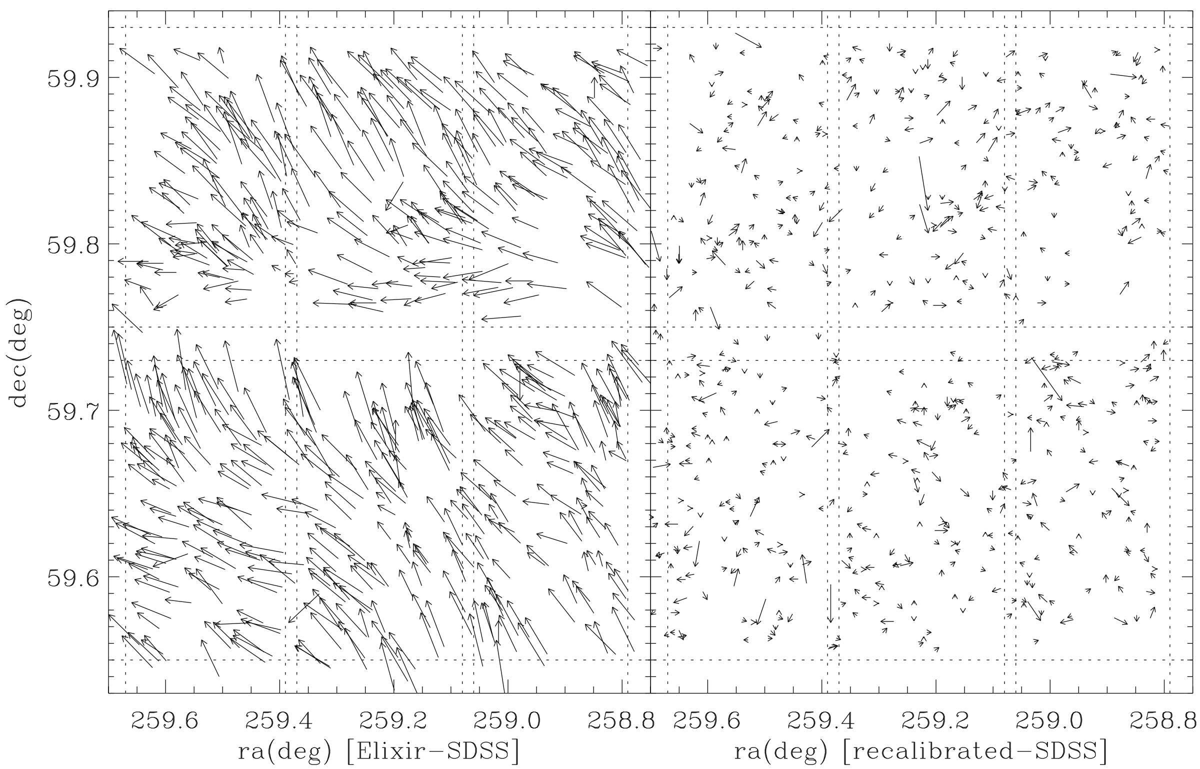

FIG. 3.— The figure shows the improvement in astrometric solutions after the astrometric calibration with SDSS sources. The vectors indicate the difference between reference SDSS positions vs detected positions. The size of the vectors are exaggerated by a factor of 250. The head of the arrows are pointing to SDSS positions. After the calibration, the size of the vectors remarkably decreased (more than a factor of 5) and the distortion is reduced significantly. The figure represents 6 adjacent CCD chips. The borders of the CCD chips are shown as dashed lines.

Basic astrometric calibrations are done using ∼50–60 USNO (United States Naval Observatory catalog; Zacharias et al. 2000) and HST GSC (Hubble Space Telescope Guide Star Catalog; Morrison et al. 2001) reference stars per chip. In this calibration, the average pixel scale and the image rotation are derived and written as WCS keywords to the header of the raw image. Since the Elixir astrometric solution uses only a first order fit, the absolute astrometric accuracy of the Elixir-processed images is about $0.''5$–$1''$ rms with respect to the reference stars above. Final processed images are delivered to us as Multiple Extension Fits files that can be manipulated using IRAF[9] `mscred`.

3.2. *Post-Elixir Processing before Mosaicking*

The delivered images are processed before mosaicking, using various IRAF packages and tasks. The post-Elixir image processing includes: (1) identification of saturated pixels and bleed trails; (2) creation of new bad pixel masks; (3) removal of satellite trails by inspecting each image frame; (4) replacement of bad pixel values; and (5) removal of cosmic rays.

As the first stage of the post-Elixir image processing, we identified saturated pixels and bleed trails using the `ccdproc` task in IRAF. The saturated pixels and bleed trails, which are the pixels showing nonlinear behavior, should be identified before stacking images because they can affect surrounding pixels during the projection of the image. Those pixels with values above the saturation level, 64000 DN for u^*-band and 62000 DN for g-band, were identified as saturated pixels. Neighboring pixels within a distance of 5 pixels along lines or columns of the selected saturation pixels are also identified as saturated. We found that the pixel saturation occurs typically at the central part of the stars brighter than $u^* \simeq 20$ mag and $g \simeq 21$ mag. Bleed trails, which result from charge spillage from a CCD pixel above its capacity, tend to run down the columns. We identify bleed trails as more than 20 connected pixels that are 5000 counts above the mean value along the whole image (i.e., setting the `ccdproc` threshold parameter as "mean+5000"). After the identification of saturated pixels and bleed trails, this information is stored as a saturation mask.

Next, we used the IRAF task `imcombine` to make new bad pixel masks by combining the saturation masks with the original CFHT bad pixel masks. The resultant masks have pixel values of 0 for good pixels, greater than 0 for bad pixels. In the bad pixel masks, we also indicate the location of satellite trails. To include satellite trails in bad pixel masks, we identified satellite trails through the visual inspection by flagging their start/end (x, y) image coordinates and widths on each CCD chip. The flagged rectangular line is then marked as bad pixels in the bad pixel masks.

With the newly constructed bad pixel masks, we fixed the bad pixels using the IRAF `fixpix` task. The value of the pixel marked in the bad pixel masks was replaced by the linear interpolation value from adjacent pixels. The next step is to identify the pixels affected by cosmic rays. We applied a robust algorithm based on a variation of Laplacian edge detection with the program, `la_cosmic` (van Dokkum 2001) on each CCD frame. This algorithm identifies cosmic rays of arbitrary sizes and shapes, and our visual inspection of this procedure confirms effective removal of cosmic rays. After the cosmic ray cleaning, we improved the astrometric solution, which is described in the next section.

[9] IRAF is distributed by the National Optical Astronomy Observatories, which are operated by the Association of Universities for Research in Astronomy, Inc., under cooperative agreement with the National Science Foundation.

3.3. *Astrometric Calibration*

The Elixir data pipeline performs a rough astrometric calibration on each image, and the existing header WCS keywords are updated with the improved astrometric solution. As mentioned in Elixir section (§3.1), Elixir calculates the astrometric solution for each CCD chip. An initial guess is determined for the image coordinate based on the initial header WCS keywords, and Elixir uses HST Guide Star Catalogs or USNO database to calculate an astrometric solution. The solution derived by Elixir is a first order fit that gives the rms scatter of $0.''5 \sim 1''$. Thus, the solution is not good enough for follow-up observations that require very accurate position information such as the multi-object spectroscopy. The accurate astrometry is also important when combining and mosaicking images, since misalignment of images can lead to a loss of signal in the combined image.

To improve the astrometric solutions, we adopted SDSS sources as reference points, and derived the astrometric solution using `msctpeak` task in `mscfinder`, which is a subpackage of the IRAF mosaic reduction package, `mscred`. The SDSS sources brighter than $r \simeq 20$ mag have an absolute astrometric accuracy of $0.''045$ rms with respect to USNO catalogs (Zacharias et al. 2000) and $0.''075$ rms against Tycho–2 catalogs (Hog et al. 2000) with an additional $0.''02 \sim 0.''03$ systematic error in both cases (Pier et al. 2003). We also considered using USNO and GSC catalogs; unfortunately, many of the USNO/GSC stars were saturated in our images, making it difficult to use them for astrometric calibration.

There are other tasks such as `msczero` and `msccmatch` for deriving the astrometric solution, but we settled on using `msctpeak`. Solutions from tasks such as `msccmatch` – which works only in `TAN` projection – are reflected in the value of `CDi_j`, `CRPIXi` header keywords. As a result, the astrometric solutions from such tasks have limitations and they do not improve the astrometric accuracy significantly. On the other hand, `msctpeak` creates a separate WCS database including a higher order fit solution from `TNX` sky projection geometry, and they are written as additional keywords such as `WATi_00j` in the FITS header using `mscsetwcs` task. The resultant astrometry of the image improved significantly over the original Elixir astrometry solution.

Ultimately, we used SDSS sources with $16 < u < 22$ mag and $17 < g < 22$ mag to calculate the astrometric solutions for the u- and g-band images, respectively. The astrometric calibration objects were inspected by eye in order to exclude heavily saturated sources. The sources used for the astrometric calibration are not restricted to stars, since the SDSS filters and CFHT u^* and g filters are similar enough that the centroiding problem is not a great concern. Including both stars and galaxies, we could get ∼90 objects per chip to derive the astrometric solution. The solutions are calculated interactively for each chip, therefore there are 36 solutions for each dither image. Functions used for the fitting are polynomials of order 3∼4, and the fitting errors are typically below $0.''1$. How the astrometric solutions fair with other data are described in a separate section (§5.1). Figure 3 demonstrates the improvement of astrometric solutions after executing the above procedure.

3.4. *Production of Mosaic Images*

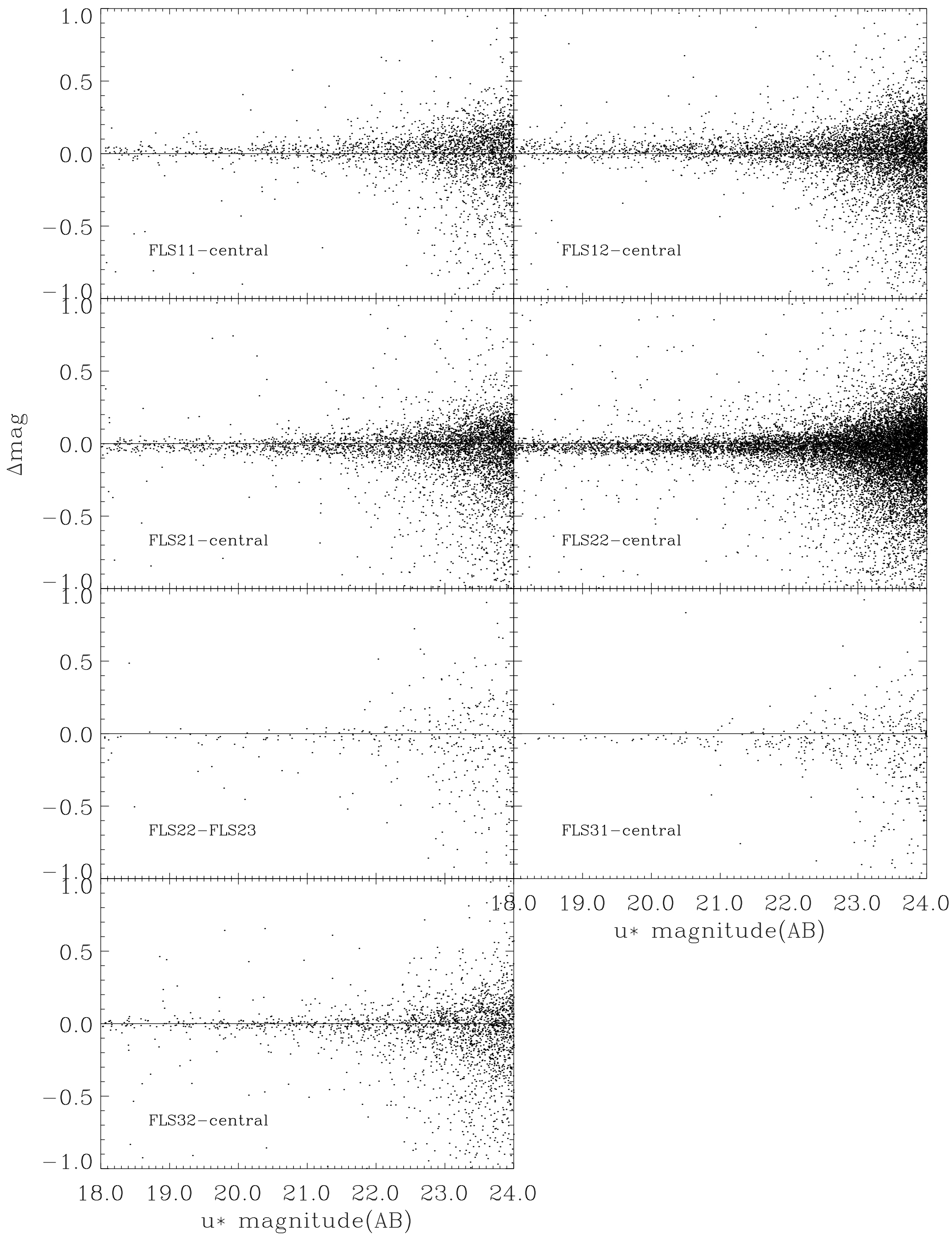

FIG. 4.— The magnitude difference of matched objects from different 8 u^*-band fields before zeropoint correction is shown. Note that the objects lying in FLS21, FLS22, and FLS31 fields are brighter than the objects lying in the central field before zeropoint correction. The mean value of the magnitude offsets are (FLS11–central)$\simeq$0.006, (FLS12–central)$\simeq$0.018, (FLS21–central)$\simeq$–0.028, (FLS22–central)$\simeq$–0.029, (FLS22–FLS23)$\simeq$–0.009, (FLS31–central)$\simeq$–0.035, and (FLS32–central)$\simeq$–0.001. Since the magnitude offsets of FLS21, FLS22, and FLS31 fields are consistent within 0.01 magnitude, we used these fields as zeropoint reference fields.

We stacked the post-Elixir processed, astrometrically calibrated images using *Swarp* software by E. Bertin at the TERAPIX (Traitment Elementaire, Reduction et Analyse des PIXels de megacam)[10]. By running *Swarp*, we created the mosaic image and the corresponding weight image (coverage map) whose pixel value is proportional to the exposure time. The reduced images were resampled, background subtracted, flux scaled, and finally coadded to one image. The interpolation function we used in the resampling is `LANCZOS3`, which uses a moderately large kernel. The pixel scale of the resampled image is kept to the original MegaCam pixel size of 0.″185. The astrometry transformation is handled by the *Swarp* program automatically, although the `TNX` WCS as derived in the previous section is not a FITS standard.

For the background subtraction, we used the background mesh size of 128 × 128 pixels, and applied 3 × 3 filter box. The background mesh size and the bin size are chosen to balance out the effect of bright stars (in general smaller than 128

[10] http://terapix.iap.fr

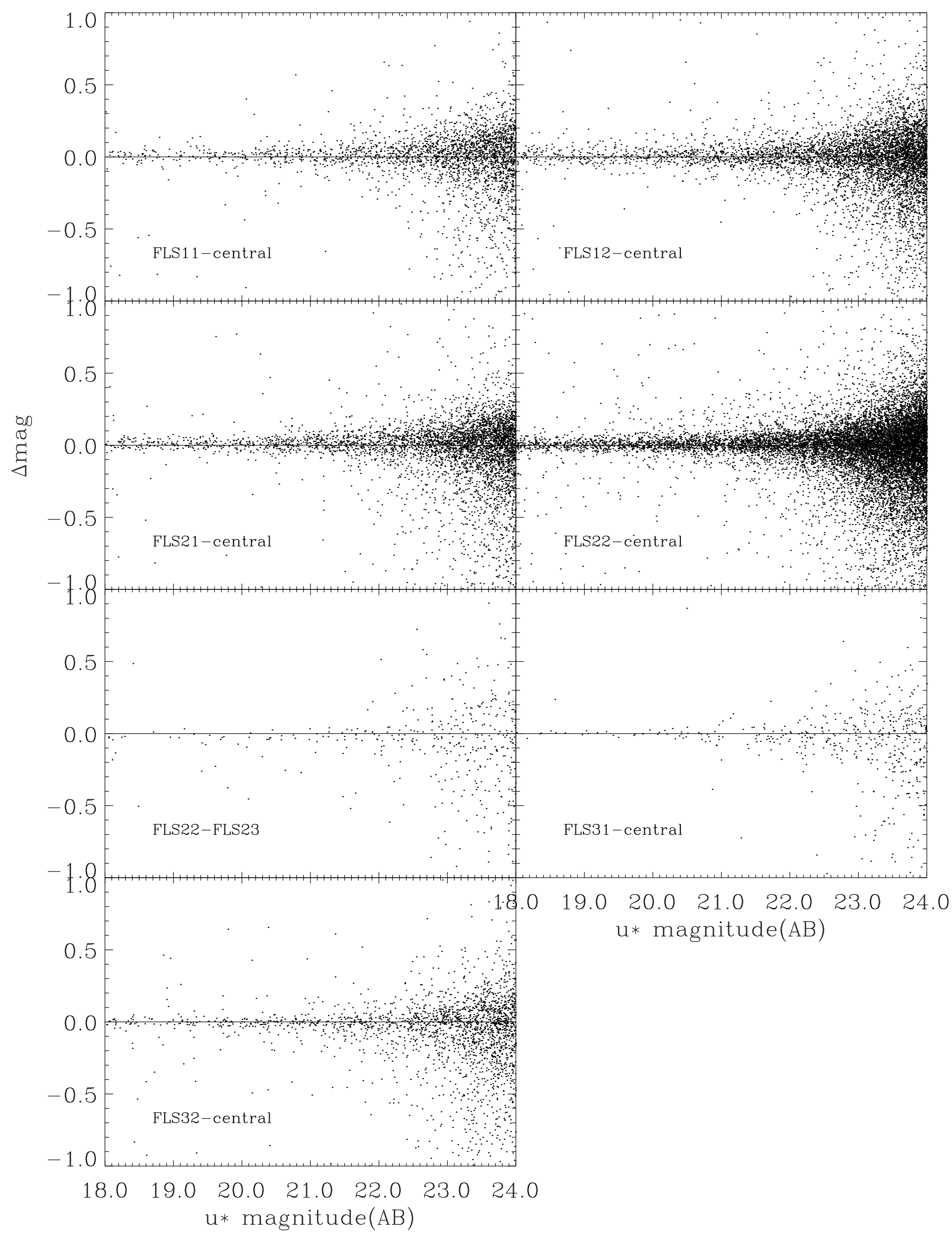

FIG. 5.— After the zeropoint correction, the magnitude differences between fields are in the order of 0.01 magnitude.

× 128 pixels) and the effect of the overall background gradient. We tried many background combinations to obtain the background as flat as possible and settled on the above parameter values. The background-subtracted images are combined by taking the weighted average of each frame. The weight images are constructed by taking the bad pixel masks, and replacing the bad pixel values to be 0, and the good pixel values to be 1. The weight images constructed this way do not account for small variation in the pixel response over the CCD (flat-field). Finally, the images are coadded using the following equation:

$$F = \frac{\sum w_i p_i f_i}{\sum w_i}$$

In this equation, F is the value of a pixel in final coadded image, w_i is the weight value for the pixel, and f_i is the value of the pixel in each individual image. The factor p_i represents the flux scale for each individual image. The images are calibrated to have the same photometric zeropoints after Elixir pipeline, but due to the airmass differences, the flux scales of the images are slightly different. In order to take into account the difference in zeropoints, we put the flux scale of the image having the least extinction to be 1.0. The flux scales of other images were calculated according to the equation:

$$p_i = 10^{\frac{k}{2.5} \times (X_i - X_0)},$$

where k is the coefficient for airmass term and X_0 and X_i are airmass values of the reference image and the image in consideration, respectively. The coadded gain of the final stacked image varies with position and is proportional to the number of frames used for producing each coadded pixel value.

3.5. *Photometric Calibration*

We performed photometric calibration on the mosaic image of each field using the photometric solution provided by the Elixir pipeline. During the production of mosaic images (§3.4), we rescaled each dither image so that each coadded image has the photometric zeropoint of the image with the least airmass value. Then, these magnitudes were corrected for the galactic extinction estimating the amount of galactic extinction from the extinction map of Schlegel et al (1998). Since the FLS field lies at moderately high galactic latitude, the amount of galactic extinction is relatively small. They are 0.15 mag and 0.1 mag on average for the u^* and g-band respectively. In the next step, we derived an additional zeropoint correction necessary to account for some of the data that were taken under non-photometric condition (e.g., thin cirrus).

To do so in u^*-band, we used fields whose mosaic image is made of photometric dither images only. The fields, FLS21, FLS22, and FLS31 are such fields, and we used them as reference photometry fields to derive photometric zeropoint correction of other u^*-band fields. Figure 4 shows the comparison of u^*-band magnitudes (before correcting for the non-photometric data) between different fields that overlap with each other. For the comparison of magnitudes, we used the total magnitude (`MAG_AUTO`) from *SExtractor* (See Section §4). In Figure 4, we can see that u^*-band magnitudes of objects in FLS21, FLS22, and FLS31 fields are slightly brighter than the same objects in the central field. Also, objects in fields other than the reference photometry fields have u^*-band magnitudes similar or fainter than those of the central field. The u^*-magnitude offsets between the central field and FLS21/22/31 are 0.03 magnitude and the rms in the offset values is of order of $\lesssim 0.01$ magnitude. This confirms that the u-band magnitudes of FLS21/22/31 fields are the most reliable. The final u^*-band zeropoint of each field are calculated using this strategy, and we present the zeropoints in Table 2. The comparison of u^*-band magnitudes of overlapping objects after the photometric calibration are presented in Figure 5. Based on the photometric consistency between FLS21/22/31, we estimate the accuracy of the u^*-band photometric zeropoint to be of order of 0.01 magnitude.

For g^*-band mosaic, we preformed photometry on dither images that are taken under photometric condition, and derived a necessary zeropoint correction by comparing the photometry of the mosaic image and the photometric reference image. The g-band zeropoint of the central field derived this way is also given in Table 2.

4. CATALOGS

4.1. *Object Detection and Photometry*

In the central 1 deg^2 region (the 03B run), the stacked u^*- and g-band images were registered to the g-band image. Both bands have the same pixel scale, so they can be easily registered with the `xregister` task in IRAF. After the registration, source catalogs were created using dual mode photometry with *SExtractor* (Bertin & Arnouts 1996). Specifically, objects are detected in the g-band image, and photometry is performed on both the g- and u^*-band images based on these positions. The weight image (coverage map) produced by *Swarp* was used as the `WEIGHT_IMAGE`. The `LOCAL` background is estimated using a 128 × 128 pixel background mesh with 3 × 3 median boxcar filtering, identical to the default *Swarp* settings.

We filter our images with a gaussian convolution kernel (`gauss_4.0_7×7.conv`) matched to our average seeing conditions (FWHM$\sim$0.″85). Finally, source detection was performed on the background-subtracted, filtered image by looking for pixel groups above the detection threshold. After playing with various parameter combinations and inspecting the results by eye, we settled on a minimum of 8 connected pixels and a 1.2σ minimum detection threshold. We also tried various values for the deblending parameter to separate ob-

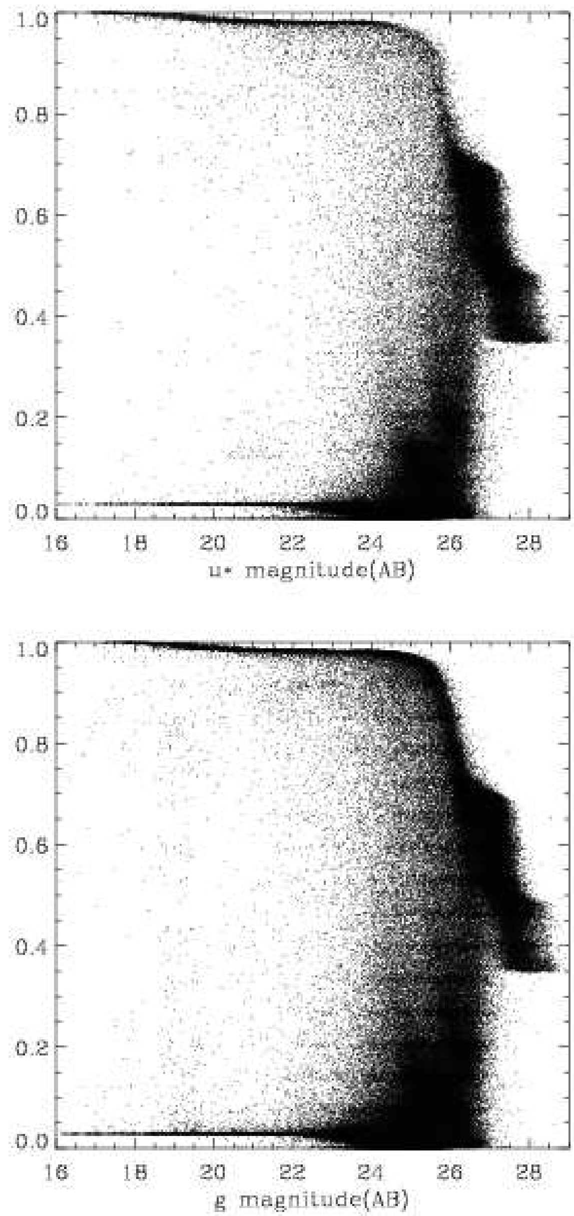

FIG. 6.— The distribution of the values of `CLASS_STAR` parameter as a function of magnitude are presented. At magnitudes below flux limit, the stellarity index of the objects are distributed between 0.35 and 0.7. The feature of the `CLASS_STAR` distribution at faint objects ($\leq$ 27 mag) is due to the difficulties when calculating stellarity index with isophotal areas of the objects.

TABLE 3
SELECTED 15 ENTRIES OF u^*/g BAND SOURCE CATALOG

obj ID	RA(J2000)	DEC(J2000)	u^*_{AUTO} [a]	ϵ	u^*_{APER} [b]	ϵ	g_{AUTO}	ϵ	g_{APER}	ϵ	$star_g$ [c]	ext_{u^*} [d]	ext_g
1001	17:14:13.301	59:15:19.199	24.992	0.051	25.016	0.042	24.726	0.066	24.699	0.052	0.010	0.120	0.088
1002	17:17:11.895	59:15:27.342	24.882	0.043	25.200	0.052	24.834	0.063	25.112	0.073	0.006	0.169	0.125
1003	17:15:52.126	59:15:26.820	24.872	0.040	25.184	0.048	24.796	0.053	25.135	0.064	0.086	0.151	0.111
1004	17:13:19.966	59:15:16.411	24.955	0.050	25.408	0.061	24.582	0.069	25.144	0.092	0.024	0.114	0.084
1005	17:19:55.115	59:15:21.739	25.356	0.080	25.615	0.070	25.364	0.064	25.744	0.063	0.928	0.141	0.104
1006	17:14:53.745	59:15:25.502	25.628	0.088	26.223	0.156	25.666	0.071	26.027	0.102	0.586	0.124	0.092
1007	17:13:55.459	59:15:21.272	25.644	0.091	26.233	0.123	25.627	0.072	26.334	0.109	0.232	0.118	0.087
1008	17:18:35.120	59:15:27.905	26.073	0.138	27.508	0.390	26.164	0.110	28.560	0.752	0.725	0.158	0.116
1009	17:15:37.141	59:15:28.592	26.565	0.189	26.240	0.122	26.578	0.181	26.348	0.128	0.693	0.146	0.107
1010	17:15:33.977	59:15:19.844	23.060	0.009	24.161	0.019	22.738	0.013	23.741	0.026	0.028	0.145	0.106
1011	17:14:33.853	59:15:19.858	23.000	0.008	23.381	0.010	22.917	0.011	23.295	0.013	0.048	0.121	0.089
1012	17:17:52.075	59:15:25.035	23.869	0.018	24.589	0.030	23.858	0.037	24.674	0.068	0.029	0.180	0.132
1013	17:18:54.719	59:15:23.401	23.485	0.013	23.992	0.016	23.444	0.015	23.960	0.019	0.959	0.148	0.109
1014	17:16:11.917	59:15:26.175	23.960	0.018	24.495	0.025	23.890	0.023	24.382	0.031	0.036	0.153	0.113
1015	17:17:19.797	59:15:29.375	26.003	0.113	26.299	0.139	26.031	0.169	26.255	0.194	0.131	0.172	0.127

[a]The AUTO magnitudes are calculated by *SExtractor*, using Kron-like elliptical aperture (Kron 1980).
[b]The APER magnitudes are calculated over a circle with 3′′ diameter.
[c]The stellarity represents CLASS_STAR calculated with *SExtractor*. The values are distributed between 0 (galaxy) and 1 (star).
[d]The galactic extinction values are calculated using the extinction map of Schlegel et al.(1998)

jects that are close together, and we adopted a deblending threshold of 32 and a deblending minimal contrast of 0.005.

Using dual mode photometry, we detect ∼200,000 sources in the central 1 deg^2 field. We also performed a single mode photometry on the u^*-band image with the same configuration file, to include u-band objects that are not detected in g-band. About ∼150 objects are detected in u^*-band without g-band detection.

We applied a nearly identical method and parameters for source detection on the seven 04A FLS u^*-band images. Since there are several very bright stars in the 04A u^*-band images, we chose a bigger background mesh size – 256 × 256 pixels to avoid the over-subtraction of the background near bright stars. Since the seeing during 04A was slightly worse than that of 03B (Table 2), we adopted a slightly larger gaussian convolution kernel (`gauss_5.0_9×9.conv`). As stated earlier, the gain for each stacked image is determined to be the original gain times the number of stacked images.

Due to interchip gaps and our 30∼40′′ dither steps, the effective exposure time varies from pixel-to-pixel. We therefore applied the *Swarp* weight image when performing photometry. Through the visual inspection of the weight image, we determined the value of `WEIGHT_THRESH` parameter for weighting in *SExtractor*. The value of the pixels in interchip gaps are measured, and used as threshold parameter value. This procedure prevents the rise of unusual sequence in the magnitude vs. magnitude error plot.

In the catalogs, we present the apparent magnitude of the objects in two different ways (aperture & total magnitude). We measured the aperture magnitude using 3′′ diameter apertures. We adopted the auto magnitude (`MAG_AUTO`) from *SExtractor* as the total magnitude, which is calculated using the Kron elliptical aperture (Kron 1980). The related parameters, `PHOT_AUTOPARAMS` were determined to be 2.5, and 3.5, which are the values in default configuration file.

4.2. *Star–Galaxy Separation*

We use the *SExtractor* stellarity index to separate star-like objects from extended sources. *SExtractor* uses 8 measured isophotal areas, peak intensity and seeing information to calculate the stellarity index. With the `SEEING_FWHM` parameter value and the neural network file as the inputs, *SExtractor*

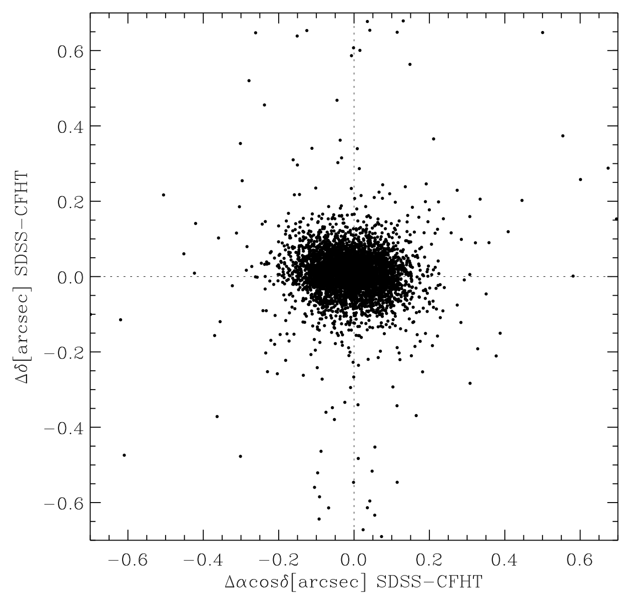

FIG. 7.— Comparison between the positions of matched objects in our g-band catalogs and SDSS g-band catalogs. Offsets are computed as SDSS minus CFHT positions.

gives the stellarity index (`CLASS_STAR`), which has values between 1 (starlike object) and 0 as the result of the classification. Figure 6 shows the distribution of stellarity index as a function of magnitude in the central 1 deg^2 field. We randomly picked objects with different apparent magnitudes and stellarity index values, and visually inspected them to see how useful the stellartiy index is for the point source vs. extended source classification. Our visual inspection reveals that bright objects ($g < 21$ mag, and $u^* < 20$ mag) with the stellarity index $\gtrsim 0.8$ are found to be stars. Through the visual inspection, we adopted the following criteria for separating point sources from extended objects:

`CLASS_STAR`$>$0.8 for 20$<u<$23
`CLASS_STAR`$>$0.8 for 21$<g<$23

In addition to these criteria, we weed out bright saturated stars ($g < 21$ mag, $u^* < 20$ mag), based on SDSS point source

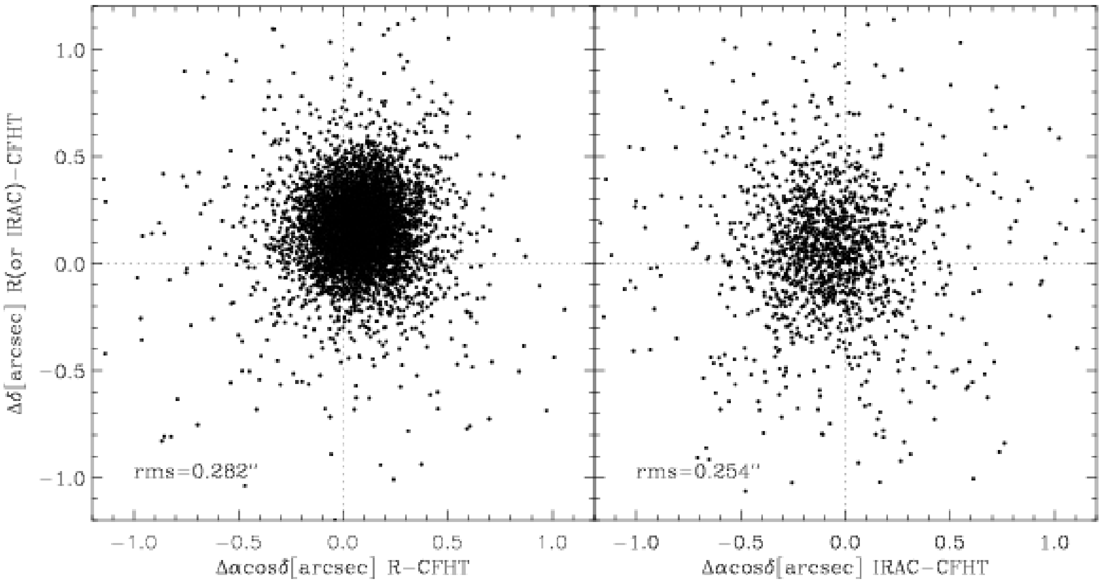

FIG. 8.— Comparison between the positions of matched objects in our u^*-band catalogs and *R*-band, IRAC catalogs. The offsets are computed as other survey minus CFHT.

catalogs. The subtraction of objects matched with SDSS stars is a good method for removing stars from our catalogs.

On the other hand, it is difficult to address the nature of faint ($g > 23$ mag, $u^* > 23$ mag) objects with the stellarity value alone, because faint, distant small galaxies are hardly resolved under 1″ seeing conditions. Fortunately, number counts tend to be dominated by galaxies at $u^*, g > 23$ mag. Therefore we do not attempt to separate stars from galaxies at these flux levels. Also, the stellarity index distribution shows a converging feature between 0.35 and 0.7 at magnitudes below flux limit ($g > 26.5$ mag, $u^* > 26.2$ mag). This is thought to be the effect of difficulties in determining isophotal areas of faint objects.

4.3. *Catalog Formats*

As an example, 15 entries of the central 1 deg^2 u^*- and g-band merged catalog is presented in Table 3. All magnitudes are given in the AB magnitude system. We include the total magnitude (MAG_AUTO) and the aperture magnitude (3″ diameter) in the catalog. The magnitudes are not corrected for the galactic extinction, but the extinction values are presented as a separate column. Magnitude errors are the outputs from *SExtractor*. Considering the error in zeropoint and the extinction correction, we believe that the minimal error in the magnitude will be about 0.02 mag. Stellarity indices are calculated in the g-band image for the central field.

5. PROPERTIES OF THE DATA

5.1. *Astrometry*

We derived the final astrometric solution using SDSS sources (both point and extended sources). The rms error between SDSS point sources and our sources are calculated to be $0.''1 < dr < 0.''15$. Considering the absolute astrometric error of 0.″1 in SDSS (Pier et al. 2003), our catalogs are thought to have the positional error of roughly 0.″15 – 0.″2. Figure 7 shows the positional differences between SDSS sources and our sources over the entire mosaic of the central 1 deg^2 field.

To address the accuracy of astrometric calibration in other ways, we compared our source positions with other available catalogs for the *Spitzer* FLS. The catalogs compared are KPNO *R*-band data (Fadda et al. 2004) and the *Spitzer* IRAC data (Lacy et al. 2005). The results are given in Figure 8. The average rms error, $dr = \sqrt{(\Delta\alpha cos\delta^2 + \Delta\delta^2)}$, is about $\sim 0.''28$ with respect to *R*-band data. *R*-band positions have a systematic offset of $\Delta\alpha = 0.''09 \pm 0.''27$ and $\Delta\delta = 0.''19 \pm 0.''31$ with respect to CFHT positions. The systematic offset is originated from the fact that the reference catalog for *R*-band data is GSC II stars, which is known to have a systematic offset with respect to SDSS reference positions (Fadda et al. 2004). Therefore, we consider the astrometry difference between *R*-band and CFHT data is well understood. For IRAC sources, the average rms error is $dr \simeq 0.''25$. The offset of IRAC positions according to CFHT positions are calculated to be $\Delta\alpha = -0.''08 \pm 0.''40$ and $\Delta\delta = 0.''04 \pm 0.''38$. The FLS IRAC data have positional accuracy of 0.″25 rms with respect to 2MASS (Lacy et al. 2005). The difference between 2MASS positions and SDSS positions caused the offset between IRAC positions and CFHT positions. The results add support to the astrometric accuracy of our dataset.

5.2. *Photometry Transformation*

As we have shown in Figure 1, MegaCam filters are slightly redder than SDSS counterparts. Therefore, we examined the correlations between u^* magnitudes and SDSS u magnitudes. To do so, we matched non-saturated point sources with $18.5 < u < 20$ from our catalog with the SDSS point source catalog, and compared the differences in their magnitudes. Figure 9 shows the comparison, and it demonstrates that the difference between the u^* and u varies from 0.1 to 0.6 magnitude as a function of the color of the object. We fitted the relation with a first order polynomial to construct the conversion formula between CFHT u^* and SDSS u-band magnitudes, and obtained the following relation from the linear least–square fitting. Although there exist some scatter, the conversion formula could be a good reference in use of CFHT u^* magnitude.

$$\Delta mag(u_{SDSS} - u_{CFHT}) =$$
$$(-0.081 \pm 0.006) + (0.237 \pm 0.004) \times (u-g)_{SDSS}$$

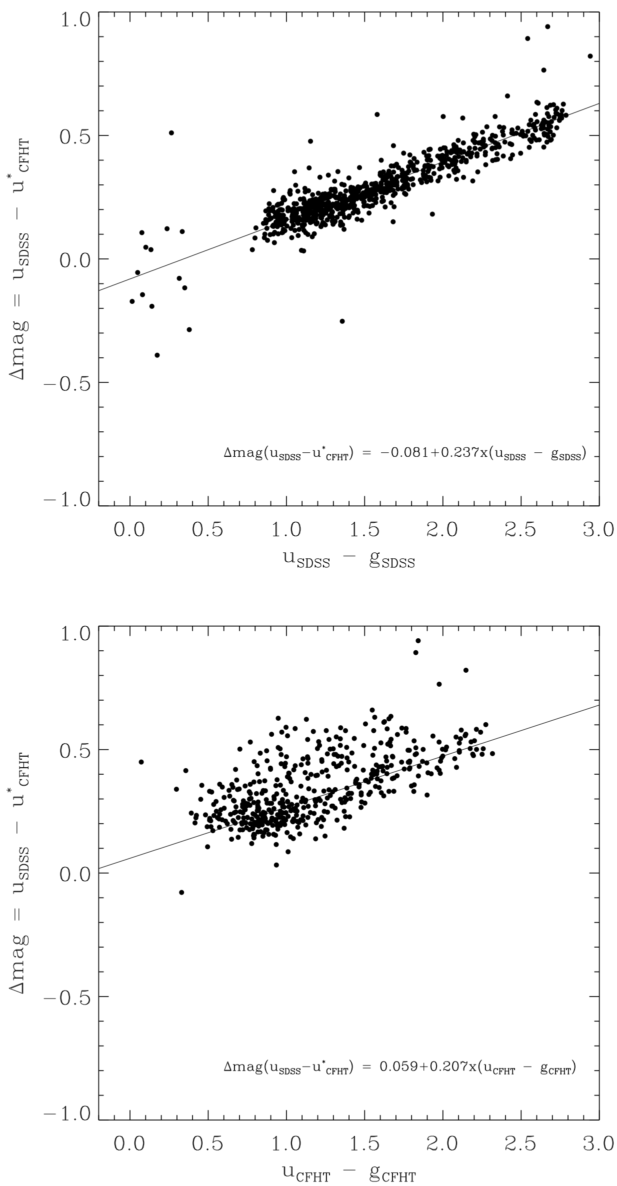

FIG. 9.— Empirical difference between CFHT u^*-band and SDSS u-band magnitudes as a function of $(u-g)$ color. We used least–square fit to find the conversion equation from one u-band to another.

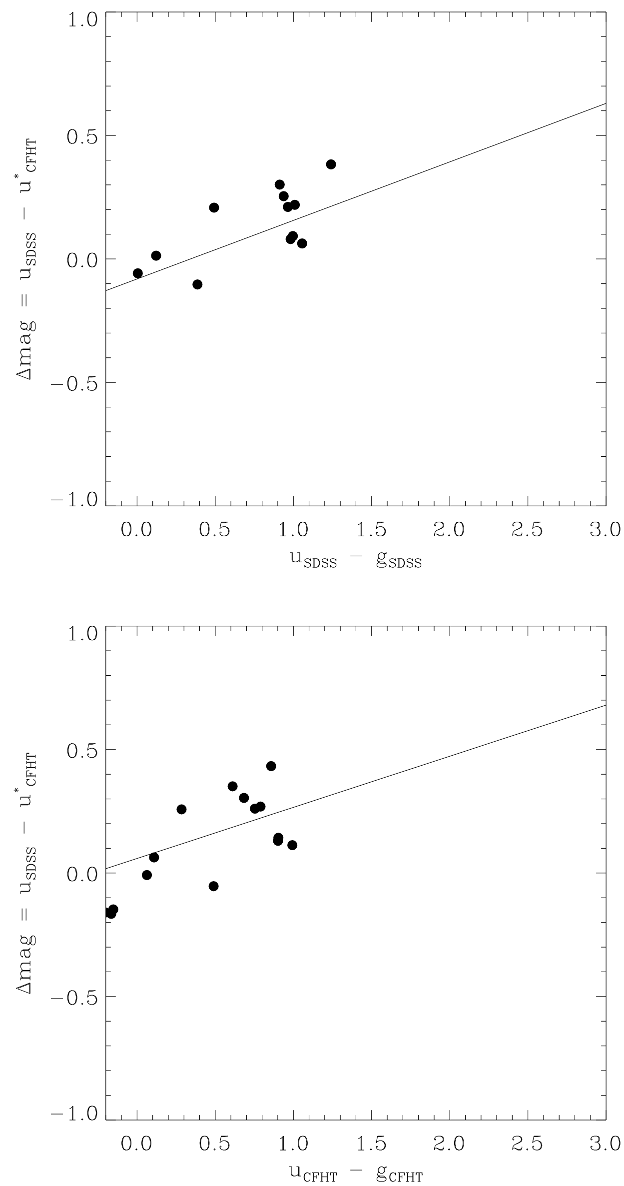

FIG. 10.— Calculated u^*-u for various spectral types of stars. The stellar templates from O5V to F9V stars were used in calculation, since in case of red stars, u-band is not good filter to sample their red colors.

We checked the above empirical relation between MegaCam u^* and SDSS u by calculating (u^*-u) vs. $(u-g)$ using the filter curves in Figure 1 and the stellar templates from O5V to F9V stars (Silva & Cornell 1992), or the empirical galaxy templates at different redshift (Coleman et al. 1980). The theoretically calculated relations of (u^*-u) vs. $(u-g)$ agree well with the empirical relations (Figure 10, 11).

On the other hand, the difference between SDSS g-band magnitude and CFHT g-band magnitude is considerably small. Figure 12 shows their difference along $(u-g)$ color. Compared to Figure 9, the magnitude difference is small (they scatters within 0.15 mag), but the differences still have a tendency of increasing toward red color. We applied least–square fit to g-band magnitude difference to find the following conversion relation.

$$\Delta mag(g_{SDSS}-g_{CFHT}) =$$
$$(-0.061\pm0.007)+(0.057\pm0.004)\times(u-g)_{SDSS}$$

5.3. *Galaxy Number Counts*

To show the depth and homogeneity of the survey, we present the galaxy number counts in u^* and g-band. The number counts are constructed for both the deep central 1 deg^2 field as well as the shallower u^*-band coverage of the entire FLS fields. Then, the results are compared with galaxy counts from other studies. The direct comparison is possible for the counts constructed from SDSS filters (Yasuda et al. 2001), while, for other studies using Johnson U, we converted the Johnson U-band magnitude to our u^* magnitude using the $u-U\simeq0.8$ conversion relation of galaxy colors from Fukugita et al. (1995), and then applying the mean of our empirical conversion relation between u^* and u ($u^*-u=0.4$ mag). For g magnitude, we used B-band number counts from the literatures (Metcalfe et al. 2000; Capak et al. 2004; Arnouts et al. 2001; Huang et al. 2001), converting B mag to g mag according to the relation of $g-B=0.3\sim0.6$ (Fukugita et al. 1995).

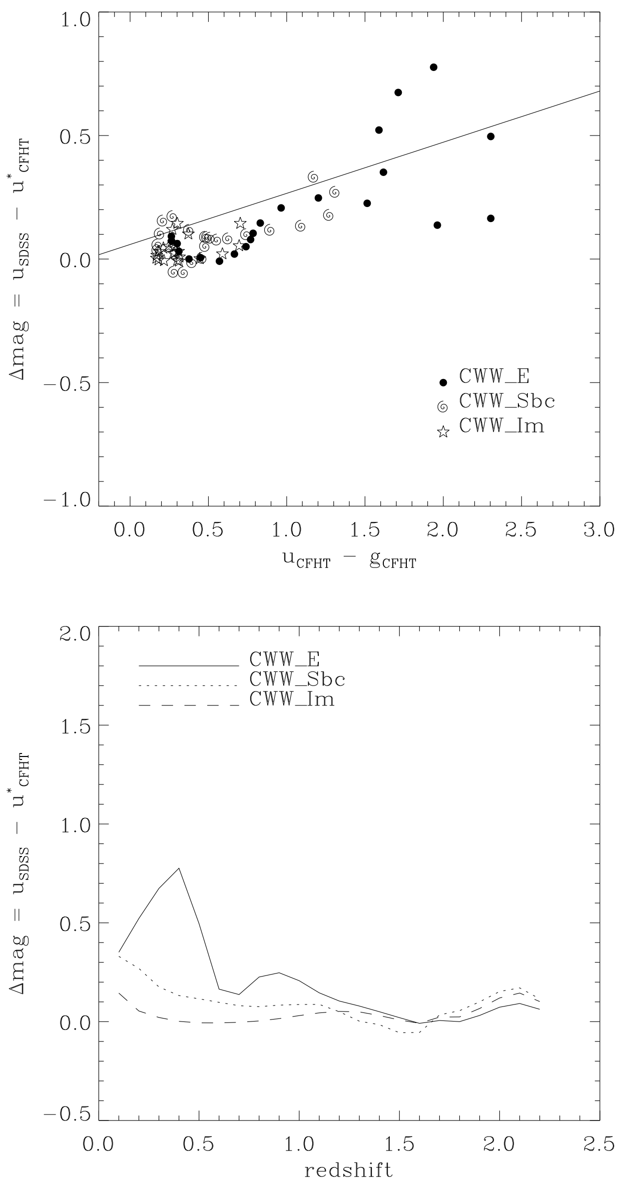

FIG. 11.— Calculated difference between the CFHT u^*-band and SDSS u-band magnitudes as a function of $(u-g)$ color. The galaxy templates used are elliptical, spiral, & irregulars from Coleman, Wu, & Weedman 1980. We redshifted the galaxies to various redshifts, and calculated their colors using filter curves.

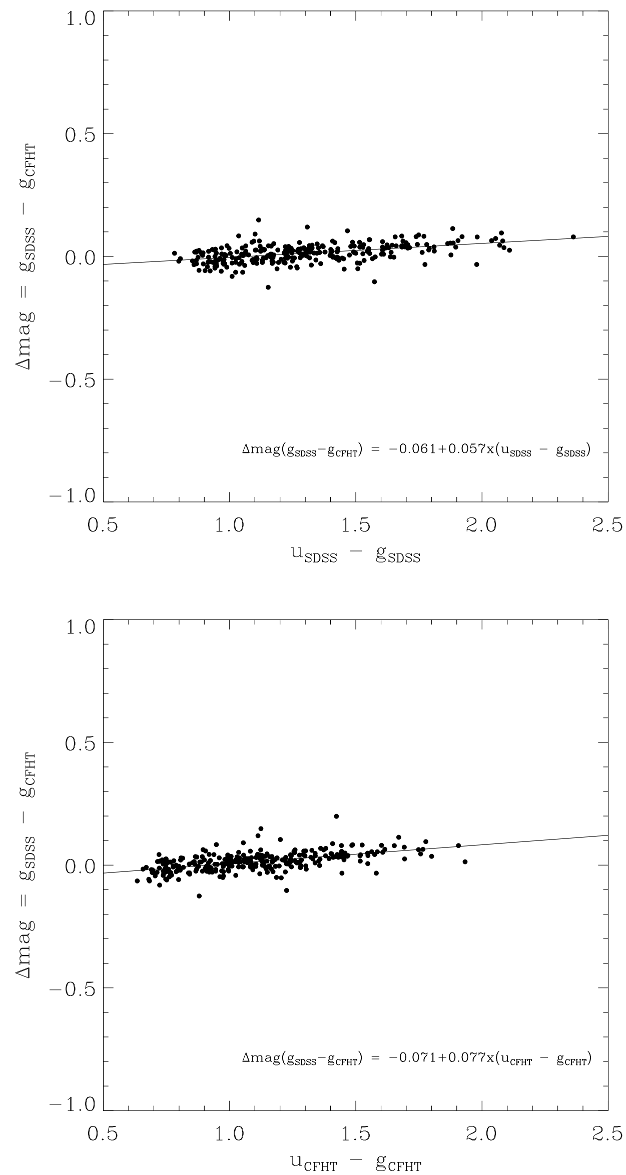

FIG. 12.— Empirical difference of CFHT g-band magnitude and SDSS g-band magnitude according to $(u-g)$ color. Because CFHT filter is redder than SDSS filter, there is also a small tendency of magnitude difference along the color. But it is not difficult to say that the difference is negligible.

The conversion relation from Johnson U to u, and from B to g filter varies according to the shape of the galaxy spectral energy distribution, so we adopt the mean difference to translate one filter to another.

The number counts are shown in Figure 13. When constructing the number counts, we excluded stellar objects using the stellarity cut introduced in section §4.2. For objects brighter than $g < 21$ mag and $u^* < 20$ mag, we matched the SDSS point source catalogs with our catalogs, and subtracted matched objects which are considered to be stars. Error bars on the figure represent the poisson errors only. Also note that our counts are not corrected for completeness.

With the exception of SDSS studies (Yasuda et al. 2001), galaxy counts are typically derived from deep, but small area surveys ($\sim$0.2–0.3 deg^2). Our image covers from 0.94 deg^2 (in case of g-band) to 5.13 deg^2 (in case of shallower u^*-band). For $u^* < 24$ mag, we include the shallower u^*-band data to maximize the area coverage. We can say that our number counts are better than other number counts in terms of the area coverage. For future use, we present a table that summarizes the result of galaxy number counts (Table 4). To construct the number counts, we use the auto magnitude in *SExtractor*. Our number counts are in good agreement with the counts from other studies to $u^* \simeq 24.8$ mag, $g \simeq 25.2$ mag. Beyond $u^* \simeq 24.8$ mag and $g \simeq 25.2$ mag, our data starts to tail off, and this shows that our u^* and g catalogs are nearly 100% complete down to the above magnitude limits. These limiting magnitudes have the uncertainty of 0.3 magnitudes due to the fluctuation in the galaxy number counts at the faint end. We also obtained the number counts for the shallower u^*-band data, the results are illustrated in Figure 14. In case of the deepest field among the shallower u^*-band, the 100% limit is 24.2 magnitude.

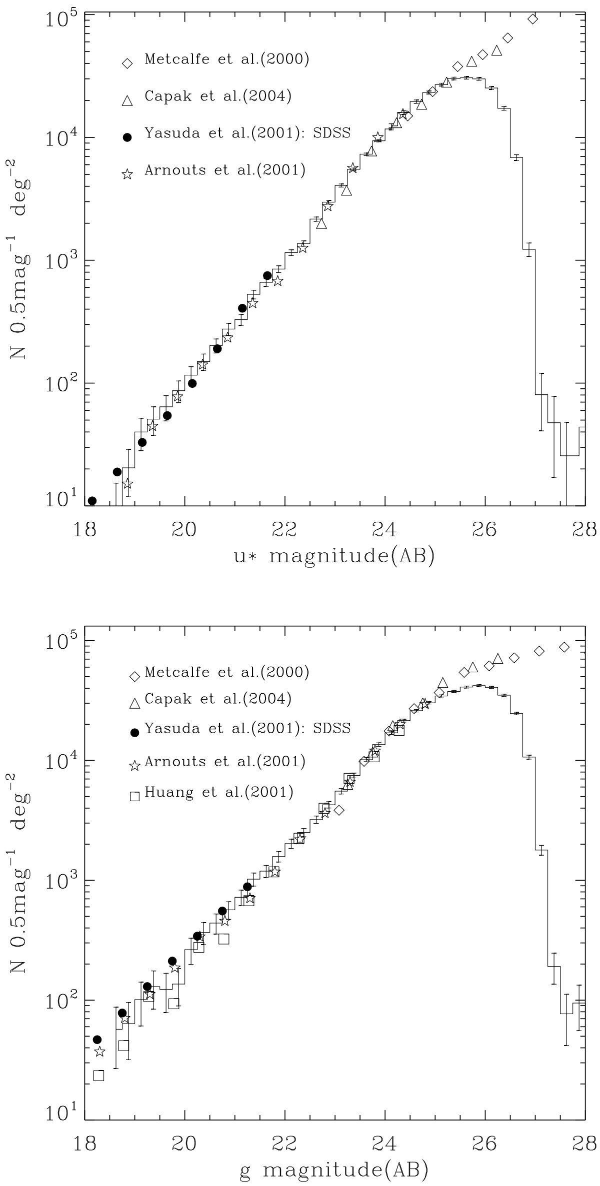

FIG. 13.— Galaxy number counts in FLS region from our u^*, g-band images. Results from other studies are overplotted. Magnitudes are in AB system.

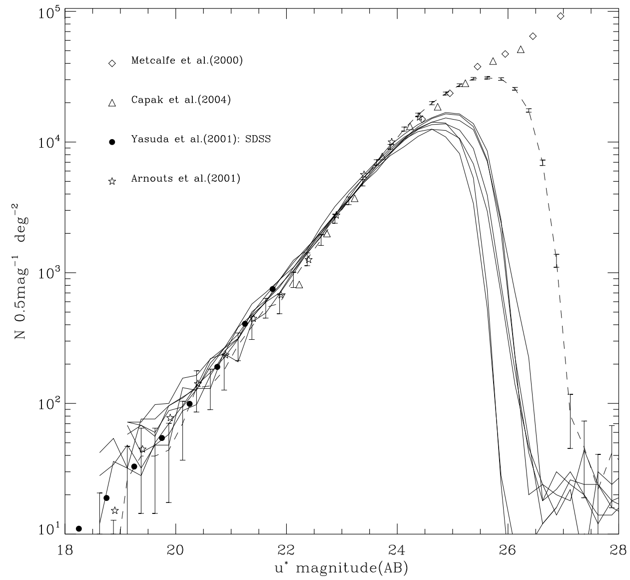

FIG. 14.— Galaxy number counts in FLS region from the shallower u^*-band images. Different solid lines indicate the different fields. The shallowest field, [FLS23] shows 100% completeness to about 23.6 magnitude. The deepest field, [FLS11] is 100% complete down to 24.2 mag. The dashed line is the result from the central 1 deg^2 region.

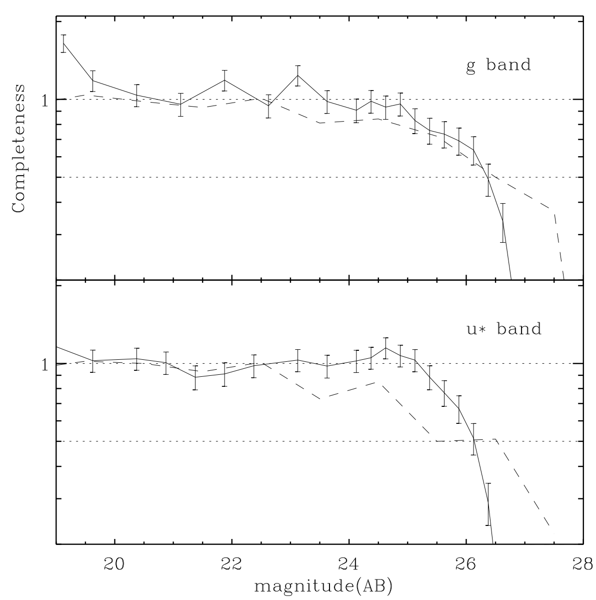

FIG. 15.— The completeness test. Completeness was inspected by dividing galaxy number counts with median number counts from other surveys (*solid* line). The *dashed* line shows the estimation of completeness from artificial image made.

5.3.1. *Completeness*

To inspect the completeness of our survey in more detail, we used two independent methods. First, we compared our galaxy counts with the deeper galaxy counts from other studies. Second, we made artificial images having the same properties with our observation (seeing, crowding, gain & background) using `artdata` package in IRAF. The artificial image contained both point sources and extended sources. The extended sources are defined to have 40 % of whole galaxies as elliptical galaxies and the remainders for disk galaxies, with minimum redshift of $z \simeq 0.01$. Poisson noise is added to the background. Then, we performed photometry with the same configuration file we used to make catalogs of observed sources. The results are shown in Figure 15, where the solid line and points indicate the completeness from the first method, and the dashed line represents the completeness estimated from the simulation. Figure 15 shows that the data is 100% complete down to $g \simeq 25.2$ mag and $u \simeq 24.8$ mag, agreeing the value found in the previous section, and is ~50% complete to 26.5 magnitude for g-band, 26.2 magnitude for u^*-band.

For the shallower u^*-band data, we examined the completeness using the first method (See Figure 16). The 50% complete limiting magnitudes are 24.8–25.4 mag, which are consistent with the estimated value in Table 2.

5.3.2. *Reliability*

TABLE 4
THE RESULT OF GALAXY NUMBER COUNTS

mag (AB)	log N_{u*} (0.5 mag^{-1} deg^{-2}) (0.5 mag^{-1} deg^{-2})	Number of Galaxies Number of Galaxies	Area Coverage (deg^2)	log N_g (0.5 mag^{-1} deg^{-2})	Number of Galaxies Number of Galaxies	Area Coverage (deg^2)
18.625	$0.933^{+0.061}_{-0.071}$	44	5.13	$1.743^{+0.060}_{-0.069}$	52	0.94
18.875	$1.272^{+0.042}_{-0.047}$	96	5.13	$1.790^{+0.057}_{-0.065}$	58	0.94
19.125	$1.555^{+0.031}_{-0.033}$	184	5.13	$1.991^{+0.046}_{-0.051}$	92	0.94
19.375	$1.659^{+0.028}_{-0.029}$	234	5.13	$2.099^{+0.041}_{-0.045}$	118	0.94
19.625	$1.760^{+0.025}_{-0.026}$	295	5.13	$2.076^{+0.042}_{-0.046}$	112	0.94
19.875	$1.891^{+0.021}_{-0.022}$	399	5.13	$2.120^{+0.040}_{-0.044}$	124	0.94
20.125	$2.017^{+0.018}_{-0.019}$	534	5.13	$2.407^{+0.029}_{-0.031}$	240	0.94
20.375	$2.127^{+0.016}_{-0.017}$	688	5.13	$2.551^{+0.025}_{-0.026}$	334	0.94
20.625	$2.258^{+0.014}_{-0.014}$	930	5.13	$2.629^{+0.023}_{-0.024}$	400	0.94
20.875	$2.392^{+0.012}_{-0.012}$	1266	5.13	$2.740^{+0.020}_{-0.021}$	516	0.94
21.125	$2.469^{+0.011}_{-0.011}$	1512	5.13	$2.844^{+0.018}_{-0.018}$	656	0.94
21.375	$2.675^{+0.009}_{-0.009}$	2426	5.13	$2.995^{+0.015}_{-0.015}$	930	0.94
21.625	$2.772^{+0.008}_{-0.008}$	3038	5.13	$3.062^{+0.014}_{-0.014}$	1084	0.94
21.875	$2.881^{+0.007}_{-0.007}$	3900	5.13	$3.184^{+0.012}_{-0.012}$	1436	0.94
22.125	$3.015^{+0.006}_{-0.006}$	5306	5.13	$3.292^{+0.011}_{-0.011}$	1840	0.94
22.375	$3.089^{+0.005}_{-0.006}$	6302	5.13	$3.385^{+0.010}_{-0.010}$	2282	0.94
22.625	$3.288^{+0.004}_{-0.004}$	9954	5.13	$3.492^{+0.008}_{-0.009}$	2920	0.94
22.875	$3.425^{+0.004}_{-0.004}$	13664	5.13	$3.616^{+0.007}_{-0.007}$	3884	0.94
23.125	$3.561^{+0.003}_{-0.003}$	18673	5.13	$3.729^{+0.006}_{-0.007}$	5042	0.94
23.375	$3.693^{+0.003}_{-0.003}$	25280	5.13	$3.860^{+0.006}_{-0.006}$	6816	0.94
23.625	$3.817^{+0.002}_{-0.002}$	33628	5.13	$3.992^{+0.005}_{-0.005}$	9224	0.94
23.875	$3.925^{+0.002}_{-0.002}$	43196	5.13	$4.118^{+0.004}_{-0.004}$	12334	0.94
24.125	$4.021^{+0.002}_{-0.002}$	53897	5.13	$4.216^{+0.004}_{-0.004}$	15464	0.94
24.375	$4.143^{+0.004}_{-0.004}$	13067	0.99	$4.320^{+0.003}_{-0.003}$	19652	0.94
24.625	$4.232^{+0.003}_{-0.003}$	16055	0.99	$4.411^{+0.003}_{-0.003}$	23648	0.94
24.875	$4.307^{+0.003}_{-0.003}$	19042	0.99	$4.506^{+0.003}_{-0.003}$	27510	0.94

We also examined the reliability of our detections. We created a negative image by multiplying –1 to the mosaic image and performed photometry on the negative image. The number of objects detected in the negative image gives us an estimate of how many false detections exist in our catalogs. The false detection rate is defined as

$$\frac{N_{false}(m, m+\Delta m)}{N(m, m+\Delta m)}$$

where $N_{false}(m, m+\Delta m)$ is the number of objects detected in the negative image over the magnitude bin of $(m, m+\Delta m)$, and $N(m, m+\Delta m)$ is the number of objects detected in the original mosaic over the same magnitude bin. The false detection rate is 0.5, when there is only noise in the image.

The number of spurious detections are relatively small (less than 0.7%) until $g \simeq 26.5$ mag and $u^* \simeq 26.0$ mag, increases steeply toward fainter magnitudes. The presence of false detections at brighter magnitudes (which is above the limiting magnitude) is due to the effects of streaks around bright stars. On the other hand, the majority of false detections at fainter magnitudes is generated from the noise. The similar tendency is emerging on the shallower u^*-band images. The false detection rate remains under 1.8% until the limiting magnitudes for the shallower u^*-band.

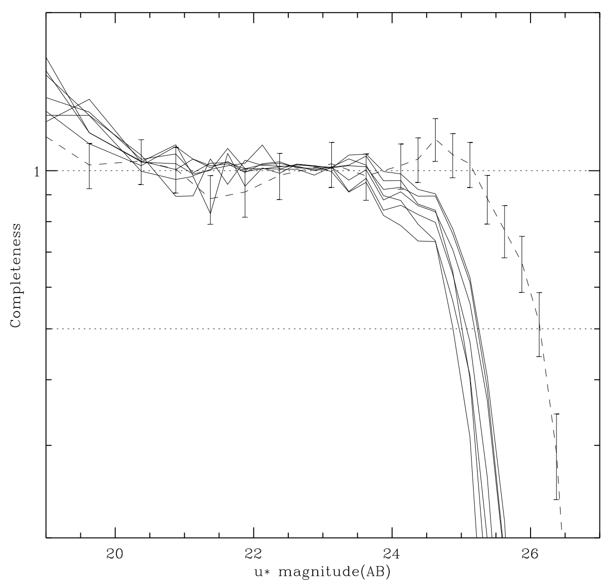

FIG. 16.— Completeness of the survey as a function of magnitude for the shallower u^*-band. The dashed line is the completeness of the central 1 deg^2 region u^*-band.

6. SUMMARY

The entire $\sim$5 deg^2 region of the *Spitzer* First Look Survey area have been observed with the MegaCam on the CFHT 3.6 m telescope. From the data, we created nine final mosaic images, photometrically and astrometrically calibrated. Two of them are the deeper u^*, g-band images on the central 1 deg^2, and the remaining seven are the shallower u^*-band images over the whole 5 deg^2. The average seeing for the central 1 deg^2 field is 0.″85, while the seeing is $\sim$1.″00 otherwise. The central field goes as deep as $g \simeq 26.5$ mag and $u^* \simeq 26.2$ mag at 5σ flux limit within 3″ aperture (or $\sim$50% completeness), while the shallower u^*-band data goes to 25.4 mag. Our data are deep enough to detect optical counterparts of many IRAC and MIPS sources in the FLS region. We recalibrated the astrometric solution, and the final absolute astrometric uncertainty is at the level of 0.″1 when compared with SDSS point sources. With other surveys on FLS, the rms error is under 0.″3, and it reflects merely the astrometric accuracy of the other datasets. The high astrometirc accuracy allows this data to be used efficiently for multislit or fiber spectroscopic observation of faint galaxies in the FLS. Using dual mode photometry, with *g*-band as the reference image, about 200,000 extragalactic objects are detected in our central 1 $\deg^2$ (effective observed area reaches $\simeq 0.94$ $\deg^2$) down to $g \simeq 26.5$ mag. There are $\sim$50,000 sources per $\deg^2$ in the shallower u^*-band images down to $u^* \simeq 25.4$ mag. Our galaxy number counts are consistent with other studies, and the number of spurious detections is less than 0.7% below our limiting magnitudes. Our data could be used in many ways: for example, i) selection of high redshift objects using broad-band dropout technique, ii) improvement of photometric redshifts, and iii) investigation on rest-frame UV properties of high redshift infrared sources. These studies are currently under way. The mosaic images and catalogs will be available through a public website in near future.

We acknowledge the FLS members for their support on this program, and Luc Simard and Tom Soifer for helping us to prepare the CFHT proposal. This work was supported by the university-institute cooperative research fund from the Korea Astronomy and Space Science Institute, and the grant No. R01-2005-000-10610-0 from the Basic Research Program of the Korea Science & Engineering Foundation. We also acknowledge the hospitality of the Korean Institute of Advanced Study during the final stage of this work, and the support from the School of Earth & Environmental Sciences Brain Korea 21 program at Seoul National University.

Facility: CFHT (MegaCam)

REFERENCES

Adelberger, K. L. & Steidel, C. C. 2000, ApJ, 544, 218
Arnouts, S. et al. 2001, A&A, 379, 740
Appleton, P. N. et al. 2004, ApJS, 154, 147
Bertin, E. & Arnouts, S. 1996, A&AS, 117, 393
Boulade, O. et al. 2003, Instrument Design and Performance for Optical/Infrared Ground-based Telescope, Proceedings of the SPIE, 4841, 72
Calzetti, D., Kinney, A. L., & Storchi-Bergmann, T. 1994, ApJ, 429, 582
Capak, P. et al. 2004, AJ, 127, 180
Choi, P. I. et al. 2005, ApJ in press (astro-ph/0509894)
Colemanm, G. D., Wu, C.-C., & Weedman, D. W. 1980, ApJS, 43, 393
Condon, J. J., Cotton, W. D., Yin, Q. F., Shupe, D. L., Storrie-Lombardi, L. J., Helou, G. Soifer, B. T., & Werner, M. W. 2003, AJ, 125, 2411
Fadda, D., Jannuzi, B., Ford, A., & Storrie-Lombardi, L. J. 2004, AJ, 128, 1
Fazio, G. et al. 2004, ApJS, 154, 10
Fang, F. et al. 2004, ApJS, 154, 35
Frayer, D. T. et al. 2004, ApJS, 154, 137
Frayer, D. T. et al. 2005, AJ, in press (astro-ph/0509649)
Fukugita, M., Shimasaku, K., & Ichikawa, T. 1995, PASP, 107, 945
Hog, E. et al. 2000, A&A, 357, 367
Huang et al. 2001, A&A, 368, 787
Kennicutt, R. C. 1998, ARA&A, 36, 189
Kron, R. G. 1980, ApJS, 43, 305
Lacy, M. et al. 2004, ApJS, 154, 166
Lacy, M. et al. 2005, ApJS, in press (astro-ph/0507143)
Madau, P., Pozzetti, L., Dickinson, M. 1998, ApJ, 498, 106
Marleau, F. R. et al. 2004, ApJS, 154, 66
Metcalfe, N., Shanks, T., Campos, A.,McCracken, H. J., Fong, R. 2001, MNRAS, 323, 795
Meurer, G. R., Heckman, T. M, & Calzetti, D. 1999, ApJ, 521, 64
Morrison, J. E. et al. 2001, AJ, 121, 1752
Oke, J. B. 1974, ApJS, 27, 21
Pier, J. R. et al. 2003, AJ, 125, 1559
Rieke, G. H. et al. 2004, ApJS, 154, 25
Schlegel, D. J., Finkbeiner, D. P., & Davis, M. 1998, ApJ, 500, 525
Silva, D. R. & Cornell, M. E. 1992, ApJS, 81, 865
van Dokkum, P. G. 2001, PASP, 113, 1420
Yan, L. et al. 2004, ApJS, 154, 60
Yan, L. et al. 2004, ApJS, 154, 75
Yasuda, N. et al. 2001, AJ, 122, 1104
Zacharias, N. et al. 2000, AJ, 120, 2131